JUSTC

Article

http://justc.ustc.edu.cn

Received: May 25, 2024; Accepted: June 02, 2024

Enhanced photocatalytic CO_2 reduction performance in Ni-doped perovskite nanocrystals controlled by magnetic fields

Zhiwen Zhang[1,2], Haoran Zhang[1,2], Huang Zhou[1,2], Yu Zhang[1,2] ✉, and Yuen Wu[1,2] ✉

[1]*Key Laboratory of Precision and Intelligent Chemistry, School of Chemistry and Materials Science, University of Science and Technology of China, Hefei 230026, China;*

[2]*Deep Space Exploration Laboratory, University of Science and Technology of China, Hefei 230026, China*

✉Correspondence: Yu Zhang, E-mail: zy11260@ustc.edu.cn; Yuen Wu, E-mail: yuenwu@ustc.edu.cn

© 2024 The Author(s). This is an open access article under the CC BY-NC-ND 4.0 license (http://creativecommons.org/licenses/by-nc-nd/4.0/).

Graphical abstract

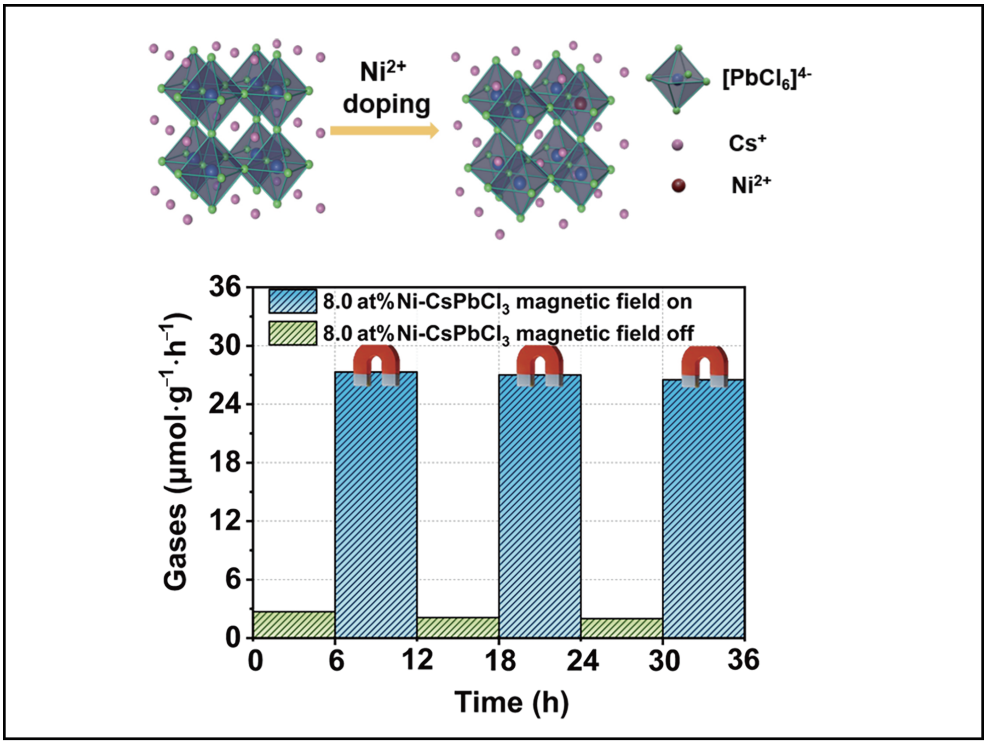

Applying an external magnetic field enhances the photocatalytic CO_2RR efficiency of Ni-doped $CsPbCl_3$.

Public summary

- This study provides an effective strategy for enhancing the efficiency of the photocatalytic carbon dioxide reduction reaction (CO_2RR) by manipulating spin-polarized electrons in photocatalytic semiconductors via a noncontact external magnetic field.
- Compared with its counterpart, Ni-doped $CsPbCl_3$ exhibits a sixfold increase in CO_2RR efficiency under a 500 mT magnetic field.
- The significant enhancement of the catalytic performance by the magnetic field is attributed to the synergistic effects of magnetic element doping and the external magnetic field, leading to reduced electron–hole recombination and extended carrier lifetimes.

Citation: Zhang Z W, Zhang H R, Zhou H, et al. Enhanced photocatalytic CO_2 reduction performance in Ni-doped perovskite nanocrystals controlled by magnetic fields. *JUSTC*, **2024**, 54(9): 0902. CSTR: 32290.14.JUSTC-2024-0078. DOI: 10.52396/JUSTC-2024-0078

JUSTC

Article

http://justc.ustc.edu.cn

Received: May 25, 2024; Accepted: June 02, 2024

Enhanced photocatalytic CO_2 reduction performance in Ni-doped perovskite nanocrystals controlled by magnetic fields

Zhiwen Zhang[1,2], Haoran Zhang[1,2], Huang Zhou[1,2], Yu Zhang[1,2] ✉, and Yuen Wu[1,2] ✉

[1]*Key Laboratory of Precision and Intelligent Chemistry, School of Chemistry and Materials Science, University of Science and Technology of China, Hefei 230026, China;*
[2]*Deep Space Exploration Laboratory, University of Science and Technology of China, Hefei 230026, China*

✉Correspondence: Yu Zhang, E-mail: zy11260@ustc.edu.cn; Yuen Wu, E-mail: yuenwu@ustc.edu.cn
© 2024 The Author(s). This is an open access article under the CC BY-NC-ND 4.0 license (http://creativecommons.org/licenses/by-nc-nd/4.0/).

Cite This: *JUSTC*, **2024**, 54(9): 0902 (8pp)

Read Online

Supporting Information

Abstract: In recent years, magnetic fields have been widely applied in catalysis to increase the performance of electrocatalysis, photocatalysis, and thermocatalysis through an important noncontact way. This work demonstrated that doping $CsPbCl_3$ halide perovskite nanocrystals with nickel ions (Ni^{2+}) and applying an external magnetic field can significantly enhance the performance of the photocatalytic carbon dioxide reduction reaction (CO_2RR). Compared with its counterpart, Ni-doped $CsPbCl_3$ exhibits a sixfold increase in CO_2RR efficiency under a 500 mT magnetic field. Insights into the mechanism of this enhancement effect were obtained through photogenerated current density measurements and X-ray magnetic circular dichroism. The results illustrate that the significant enhancement in catalytic performance by the magnetic field is attributed to the synergistic effects of magnetic element doping and the external magnetic field, leading to reduced electron–hole recombination and extended carrier lifetimes. This study provides an effective strategy for enhancing the efficiency of the photocatalytic CO_2RR by manipulating spin-polarized electrons in photocatalytic semiconductors via a noncontact external magnetic field.

Keywords: photocatalysis; carbon dioxide reduction reaction (CO_2RR); perovskite; spin polarization; magnetic field

CLC number: O643.3 **Document code:** A

1 Introduction

Over the past three centuries, the extensive use of fossil fuels has led to direct CO_2 emissions exceeding 33 billion tons annually, posing significant risks to climate and environmental stability[1–4]. Photocatalytic CO_2 conversion into fuels and chemicals is a promising solution for reducing atmospheric CO_2 levels and potentially initiating an artificial carbon cycle[5]. Despite progress, challenges in terms of reaction activity and selectivity persist in practical applications. This is due mainly to complex processes involving photon absorption, electron–hole pair dynamics, and CO_2 activation on catalyst surfaces. Ongoing studies aim to optimize these steps to increase the photocatalytic CO_2 reduction efficiency[6–8].

Since Miyasaka's 2009 research on halogenated perovskites for solar cells[9], these materials have attracted widespread interest in optoelectronics and energy conversion[10,11]. Perovskite materials are widely used in photocatalytic CO_2 reduction[12–14], which can be attributed to their high light absorption coefficients, tunable bandgaps, and long carrier transport distances[15,16]. However, owing to the high quantum efficiency of perovskite materials, the recombination of photogenerated carriers is increased, which is an undesirable outcome of the photocatalytic process[17,18]. To address this, strategies such as the construction of heterojunctions have been employed to facilitate the spatial separation of charge carriers and reduce recombination, thereby increasing photocatalytic efficiency[19–25]. However, heterojunction materials may encounter challenges, including complex synthesis[26], interface defects[27,28], and lattice mismatch[29], which may complicate the manufacturing process and harm the ability to achieve stable catalytic performance.

Compared with enhancing catalytic performance through material fabrication, magnetic fields offer advantages such as being noncontact, easy to apply, and capable of stably boosting catalytic efficiency. For this reason, magnetic fields have attracted increasing attention in catalysis. For example, Pan et al. reported that the yield of the electrocatalytic carbon dioxide reduction reaction (CO_2RR) to formic acid doubled after a magnetic field was applied, which was attributed to the modulation of the radical-to-spin state[30]. Extensive research efforts have been devoted to uncovering the underlying reaction mechanisms facilitated by magnetic fields, with a focus on theories of spin polarization and electromagnetism[31–34]. During electron transport, interactions between electrons and the lattice structure lead to energy losses of photogenerated carriers, thus reducing transport efficiency. To address this issue, modulating electron spin polarization has been identified as an effective method to mitigate energy loss[35]. After doping with magnetic elements, the application of an external magnetic field can reverse the direction of electron spin through orbital coupling interactions, thereby reducing electron collisions and subsequent energy loss. Such adjustments

CSTR: 32290.14.JUSTC-2024-0078
DOI: 10.52396/JUSTC-2024-0078
JUSTC, **2024**, 54(9): 0902

in electron spin polarization are crucial for improving catalytic efficiency[36,37].

The enhancement of the photocatalytic CO_2 reduction efficiency in halide perovskite nanocrystals through the manipulation of spin-polarized electrons via a magnetic field was explored in this study. By doping Ni ions into the material, spin polarization bands were created. Under a 500 mT magnetic field, the photocatalytic efficiency increases sixfold. The underlying mechanism was investigated through photocurrent measurements and X-ray magnetic circular dichroism (XMCD) analysis. This significant improvement is attributed to the extended lifespan of spin-polarized photogenerated carriers and reduced charge recombination. These findings underscore the effectiveness of using external magnetic fields to control spin-polarized electrons in magnetically doped semiconductors, presenting a noncontact and environmentally friendly strategy to optimize photocatalytic CO_2 reduction. This work not only advances the understanding of the effects of magnetic fields on photocatalysis but also opens new avenues for developing high-efficiency, eco-friendly catalysts for mitigating climate change.

2 Materials and methods

2.1 Chemicals

All chemicals were used as received without further purification. The materials used included cesium carbonate (Cs_2CO_3, 99%, Innochem), lead(II) chloride ($PbCl_2$, AR, SCRC), anhydrous nickel chloride ($NiCl_2$, 98%, Aladdin), 1-octadecene (ODE, 90%, Sigma–Aldrich), oleic acid (OA, AR, SCRC), oleylamine (OAm, 70%, Sigma–Aldrich), and hexane (AR, SCRC).

2.2 Synthesis of catalysts

Cs_2CO_3 (407 mg) was combined with ODE (18 mL) and OA (1.75 mL) in a 50 mL 3-neck round-bottom flask and heated to 120 °C for 1 h under vacuum. The mixture was then purged with nitrogen and heated to 150 °C until all Cs_2CO_3 reacted with OA, forming Cs-oleate. The Cs-oleate was obtained and kept for further use. $PbCl_2$ (69.0 mg) and $NiCl_2$ (128.6 mg) were mixed with ODE (10 mL), OA (3 mL), OAm (3 mL), and HCl (20 μL) in a 50 mL 3-neck flask and dried under vacuum at 120 °C for 1 h. This mixture was then heated to 200 °C under an argon atmosphere. Then, the Cs-oleate (4 mL) was swiftly injected into the heated solution, and after 5 s, the solution was cooled via an ice bath (Fig. S1). After centrifugation, the catalyst was washed three times with acetone and absolute ethanol. The synthesis methods of catalysts with other Ni doping ratios are similar, and the dosages of $PbCl_2$ and $NiCl_2$ need to be adjusted.

2.3 Characterizations

X-ray diffraction patterns of the samples were recorded on a Rigaku Miniflex-600 with Cu Kα radiation (λ = 0.15406 nm). Transmission electron microscopy (TEM) was performed with a Hitachi-7700. High-resolution TEM and high-angle annular dark-field scanning TEM images were recorded via a Talos F200X. X-ray photoelectron spectroscopy (XPS) was performed via Al Kα radiation on a scanning X-ray microprobe (PHI 5000 Verasa, ULAC-PHI, Inc.). X-ray magnetic circular dichroism (XMCD) analysis was performed at the BL12B beamline of the National Synchrotron Radiation Laboratory (NSRL, Hefei).

2.4 Photocatalytic CO_2 reduction reaction

Thin films of $CsPbCl_3$ and Ni-$CsPbCl_3$ were prepared on quartz substrates for the photocatalytic CO_2RR. The substrates were first cleaned with acetone twice and heated to 70 °C. The catalyst was dispersed in hexane and spray-coated on heated quartz substrates; subsequently, the coated substrates were heated to 80 °C in a vacuum drying oven for 1 h to remove the surface ligands. The weight of the thin films of $CsPbCl_3$ and Ni-doped $CsPbCl_3$ on quartz was approximately 5.0 mg. After drying, the thin films were placed into a photocatalytic reactor (Perfect Light PQ256) to conduct the photocatalytic CO_2RR. Before the photocatalytic CO_2 reduction reaction, the reactor was degassed to remove air, and H_2O-saturated CO_2 was purged into the reactor for 1 h. AM 1.5G 150 mW/cm^2 (Perfect Light PLS-SXE 300) was placed on the top of the reactor as a light source. After the photocatalytic CO_2RR, the products were collected and analyzed via GC (Panna A91). For the experiments under an external magnetic field, permanent magnets were placed under the reactor (Fig. S2).

3 Results and discussion

3.1 Characterizations of the catalyst

To introduce spin-polarized electrons in halide perovskites, magnetic Ni ions were doped into the all-inorganic perovskite $CsPbCl_3$, effectively substituting for Pb sites (Fig. 1a). Both $CsPbCl_3$ and Ni-doped $CsPbCl_3$ (denoted as Ni-$CsPbCl_3$) were synthesized via the conventional thermal injection method[38,39]. The nickel doping concentration was determined to be 8.0 atomic percent (at%) through inductively coupled plasma spectroscopy (ICP) (Table S1). The structural and morphological characteristics of Ni-$CsPbCl_3$ were analyzed via transmission electron microscopy (TEM) and high-resolution transmission electron microscopy (HR-TEM). The TEM image reveals the cubic morphology of Ni-$CsPbCl_3$, which is approximately 100 nm in size (Fig. 1b). The HR-TEM image shows that the crystal structure corresponds to the cubic phase (002) Miller plane of the perovskite, with a plane spacing of 0.28 nm (Fig. 1c). Additionally, high-angle annular dark-field scanning transmission electron microscopy (HAADF-STEM) with energy-dispersive X-ray spectroscopy (EDS) element mapping confirmed the uniform distribution of Ni ions within the structure (Fig. 1d, e).

The crystal structures of $CsPbCl_3$ and Ni-$CsPbCl_3$ were analyzed via X-ray diffraction (XRD) (Fig. 2a). Both materials exhibit the cubic phase of three-dimensional perovskites, which is consistent with earlier HR-TEM results. Notably, Ni-$CsPbCl_3$ shows lattice contraction due to the substitution of larger lead ions (Pb^{2+} with an ionic radius of 1.19 Å) for smaller nickel ions (Ni^{2+} with an ionic radius of 0.69 Å), resulting in a peak shift toward higher angles by approximately 0.1° [40]. The shift in the peak position demonstrates a change in the lattice constant, indicating that nickel ions have entered the

CSTR: 32290.14.JUSTC-2024-0078
DOI: 10.52396/JUSTC-2024-0078
JUSTC, **2024**, 54(9): 0902

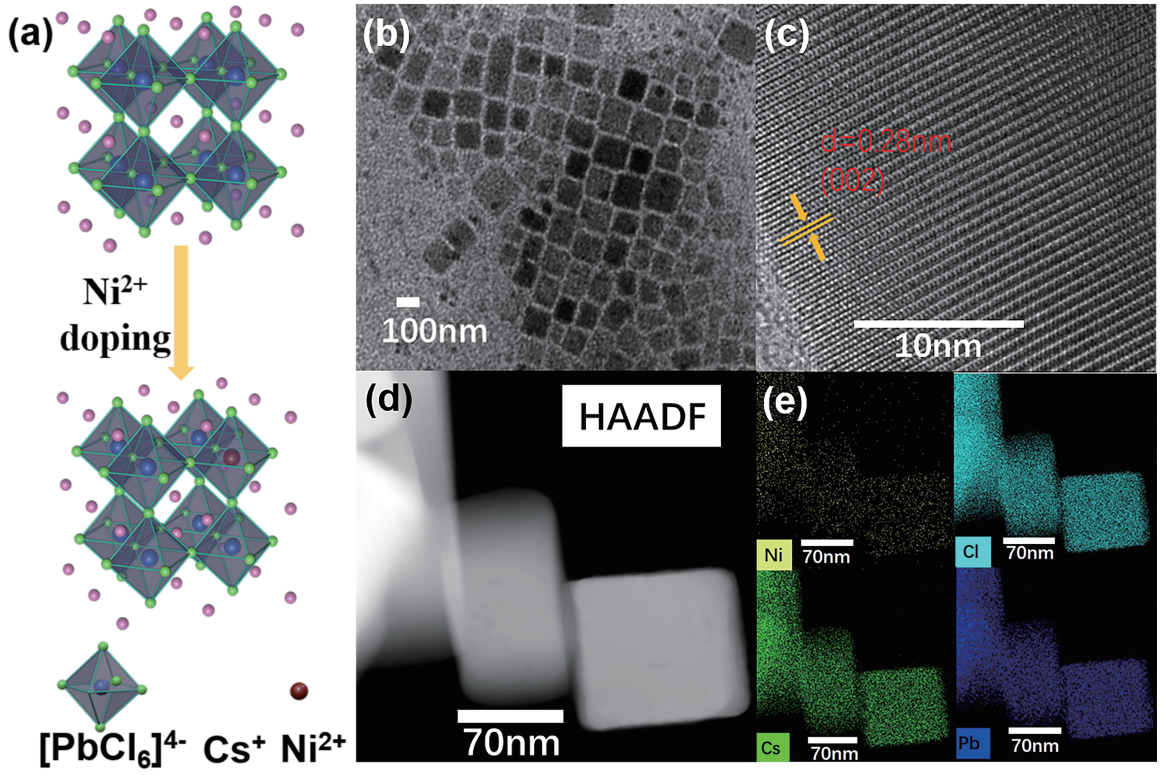

Fig. 1. (a) Schematic representation of the crystal lattice structures of $CsPbCl_3$ and Ni-$CsPbCl_3$. (b) TEM image, (c) HR-TEM image, (d) HAADF image, and (e) EDS elemental scans of Ni-$CsPbCl_3$ with a nickel doping ratio of 8.0 at%.

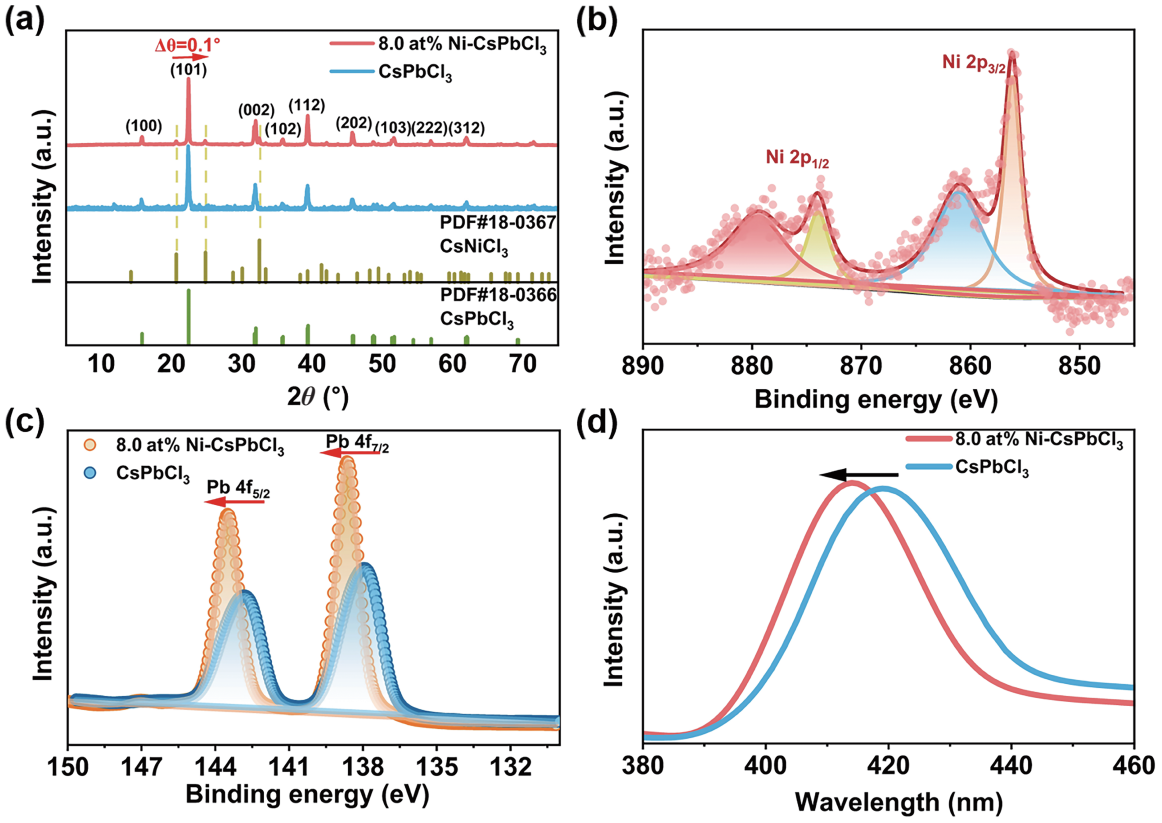

Fig. 2. (a) XRD patterns of $CsPbCl_3$ and Ni-$CsPbCl_3$ with a nickel doping ratio of 8.0 at%. (b) XPS spectrum of Ni 2p for Ni-$CsPbCl_3$ with a nickel doping ratio of 8.0 at%. (c) XPS spectra of Pb 4f. (d) PL spectra of $CsPbCl_3$ and Ni-$CsPbCl_3$ with a nickel doping ratio of 8.0 at%.

CSTR: 32290.14.JUSTC-2024-0078
DOI: 10.52396/JUSTC-2024-0078
JUSTC, **2024**, 54(9): 0902

lattice. In addition, peaks corresponding to the $CsNiCl_3$ phase appear after doping. X-ray photoelectron spectroscopy (XPS) was used to analyze the valence state of nickel. The consistency between the normalized XPS spectra of Ni 2p for Ni-$CsPbCl_3$ and NiO indicates that the Ni ions are divalent (Fig. 2b and Fig. S3)[41,42]. In addition, the binding energy peaks of Pb $4f_{5/2}$ and $4f_{7/2}$ shift toward higher energies after doping (Fig. 2c)[43–45]. The XRD and XPS results confirmed the successful doping of Ni^{2+}. Photoluminescence (PL) analysis revealed a shift in the exciton emission peak from 420 nm in $CsPbCl_3$ to 416 nm in Ni-$CsPbCl_3$, indicating that nickel doping also affects the optical properties, resulting in a slight increase in the bandgap (Fig. 2d)[46,47].

3.2 Photocatalytic carbon dioxide reduction performance

To explore the influence of various Ni doping concentrations on the yield of the photocatalytic CO_2RR, Ni-$CsPbCl_3$ samples with Ni doping ratios of 0, 0.9 at%, 4.8 at%, 5.8 at%, 8.0 at%, and 9.1 at% were synthesized by adjusting the feed ratios of $NiCl_2$ to $PbCl_2$ (Table S1). In these experiments, the product of the photocatalytic CO_2RR is carbon monoxide (CO). There is no product when argon gas is injected without carbon dioxide, which confirms that the carbon source of the product is indeed carbon dioxide (Fig. S4). Without a magnetic field, increasing the Ni doping ratio results in a slight increase in the CO yield, from 2 to 4.0 $\mu mol \cdot g^{-1} \cdot h^{-1}$ for 0 and 9.1 at% Ni (Fig. 3a), which is consistent with previously reported studies (Table S2). However, when a 500 mT magnetic field is applied, the photocatalytic performance of Ni-$CsPbCl_3$ is markedly enhanced, whereas the CO yield of $CsPbCl_3$ remains unchanged. This suggests that the catalytic enhancement induced by the magnetic field is related to Ni doping. Under the influence of the magnetic field, the CO yields for Ni doping ratios of 0.9 at%, 4.8 at%, 5.8 at%, 8.0 at%, and 9.1 at% increase by 2.8, 4.9, 5.5, 7.2, and 5.7 times, respectively. The highest observed yield was 27.3 $\mu mol \cdot g^{-1} \cdot h^{-1}$, with a nickel doping ratio of 8.0 at%. However, at a nickel doping ratio of 9.1 at%, the yield decreases. The above results suggest that increasing Ni doping contributes to improving the magnetic field enhancement of the photocatalytic reaction yield; however, excessive Ni doping leads to a decrease in this enhancement effect. Furthermore, the UV–visible absorption spectra show a blueshift in the absorption peak of Ni-$CsPbCl_3$ with increasing Ni content, indicating a corresponding increase in the bandgap width (Fig. 3b). The bandgap of $CsPbCl_3$ was estimated to be 2.80 eV via the Tauc plot method, whereas for Ni doping ratios of 9.1 at%, the bandgap increased to 3.05 eV (Fig. S5)[48]. A wider bandgap width may hamper the excitation of photogenerated

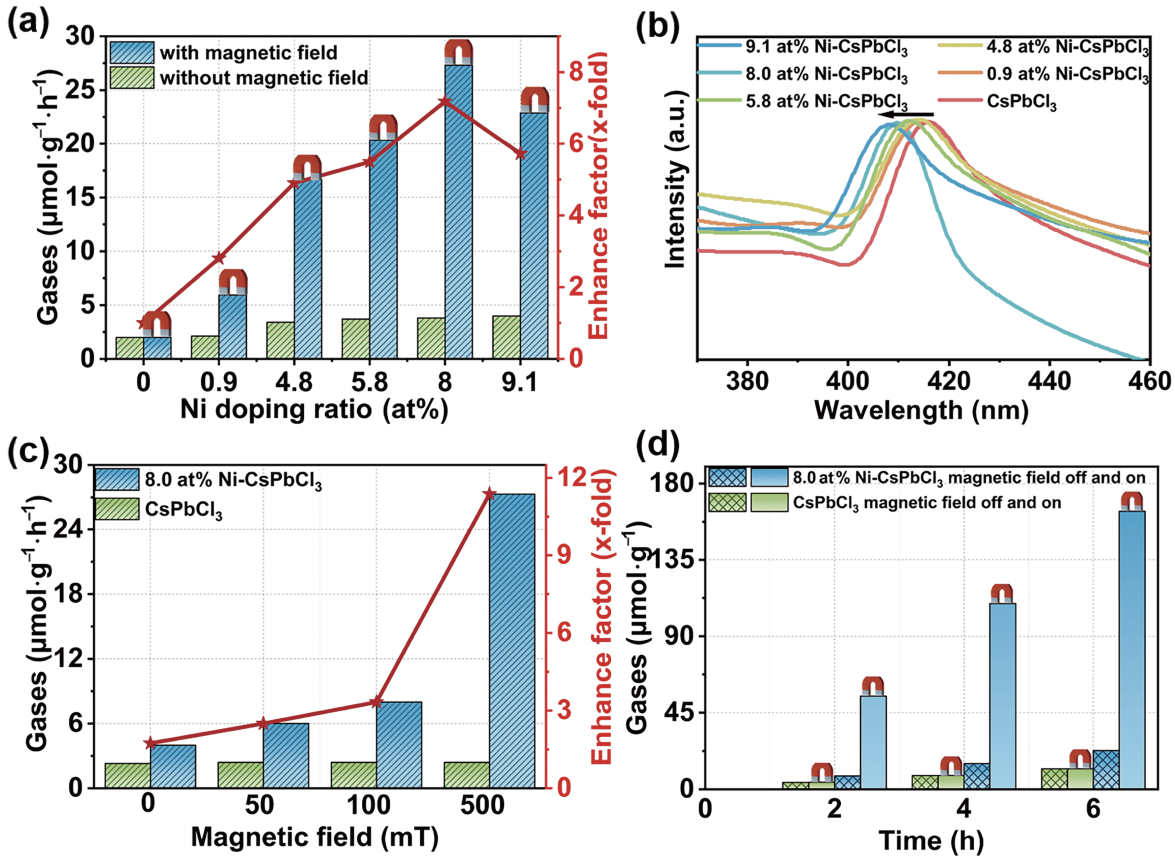

Fig. 3. (a) Photocatalytic CO_2RR product yields of Ni-$CsPbCl_3$ with various Ni doping ratios under conditions without or with an external magnetic field. (b) UV–visible absorption spectra of Ni-$CsPbCl_3$ with different Ni doping ratios. (c) Relationships between the photocatalytic CO yield and magnetic field intensity for $CsPbCl_3$ and Ni-$CsPbCl_3$ with a nickel doping ratio of 8.0 at%. (d) Changes in the photocatalytic CO yield over time for $CsPbCl_3$ and Ni-$CsPbCl_3$ with a nickel doping ratio of 8.0 at%.

CSTR: 32290.14.JUSTC-2024-0078
DOI: 10.52396/JUSTC-2024-0078
JUSTC, **2024**, 54(9): 0902

electrons, resulting in a lower catalytic performance for Ni-$CsPbCl_3$ at 9.1 at% doping ratio. When the Ni doping level increased to 9.0 at%, the presence of a more obvious $CsNiCl_3$ phase in the catalyst leads to phase separation of the catalyst (Fig. S6), whereas $CsNiCl_3$ has no catalytic activity or diamagnetism, which may weaken the enhancement effect of the magnetic field. Therefore, 8.0 at% was selected as the optimal doping ratio of Ni-$CsPbCl_3$ for the following experiments. Fig. 3c shows a positive correlation between the photocatalytic CO yield and the intensity of the magnetic field for Ni-$CsPbCl_3$, whereas no such trend is observed for $CsPbCl_3$. This further illustrates that the significant enhancement in the photocatalytic CO_2RR performance is attributed to the application of the magnetic field. Fig. 3d shows the linear accumulation of the photocatalytic products over time. This result confirms the stability and ongoing effectiveness of the magnetic enhancement on the photocatalytic performance.

To evaluate the stability of the magnetic field enhancement effect, magnetic field switch cycles were applied in the photocatalytic CO_2RR process. The efficiency of the photocatalytic CO_2RR changes rapidly and consistently with repeated switching of the magnetic field over 36 h cycles, demonstrating the repeatability of the magnetic field enhancement effect (Fig. 4a). These results confirm the stability and repeatability of the magnetic field in increasing the photocatalytic efficiency. The hysteresis loop for Ni-$CsPbCl_3$ with a nickel doping ratio of 8.0 at% shows minimal hysteresis (Fig. 4b), demonstrating a rapid response and high sensitivity to the magnetic field switch. The results of the electron paramagnetic resonance (EPR) characteristics and XRD patterns before and after the 36 h reaction show that the magnetic responsiveness and crystal structure of the material remain almost unchanged from those before the reaction (Fig. 4c, d and Fig. S7), indicating the catalytic stability of the material during the prolonged reaction. The above results confirm the stability of the magnetic field enhancement effect.

3.3 Mechanistic study

The photogenerated currents for Ni-$CsPbCl_3$ were measured both with and without an applied magnetic field to elucidate the underlying mechanisms of the magnetic field-enhanced photocatalytic CO_2RR in Ni-$CsPbCl_3$. The application of a magnetic field significantly increases the photogenerated current density of Ni-$CsPbCl_3$, with this enhancement persisting over ten cycles (Fig. 5a). This suggests that the improvement in the photocatalytic CO_2RR efficiency can be attributed to the enhanced current photogenerated by the magnetic field, which may be due to the reduction in charge carrier recombination. The EPR spectrum of Ni-$CsPbCl_3$ shows a distinct signal at approximately 330 mT, corresponding to a g factor

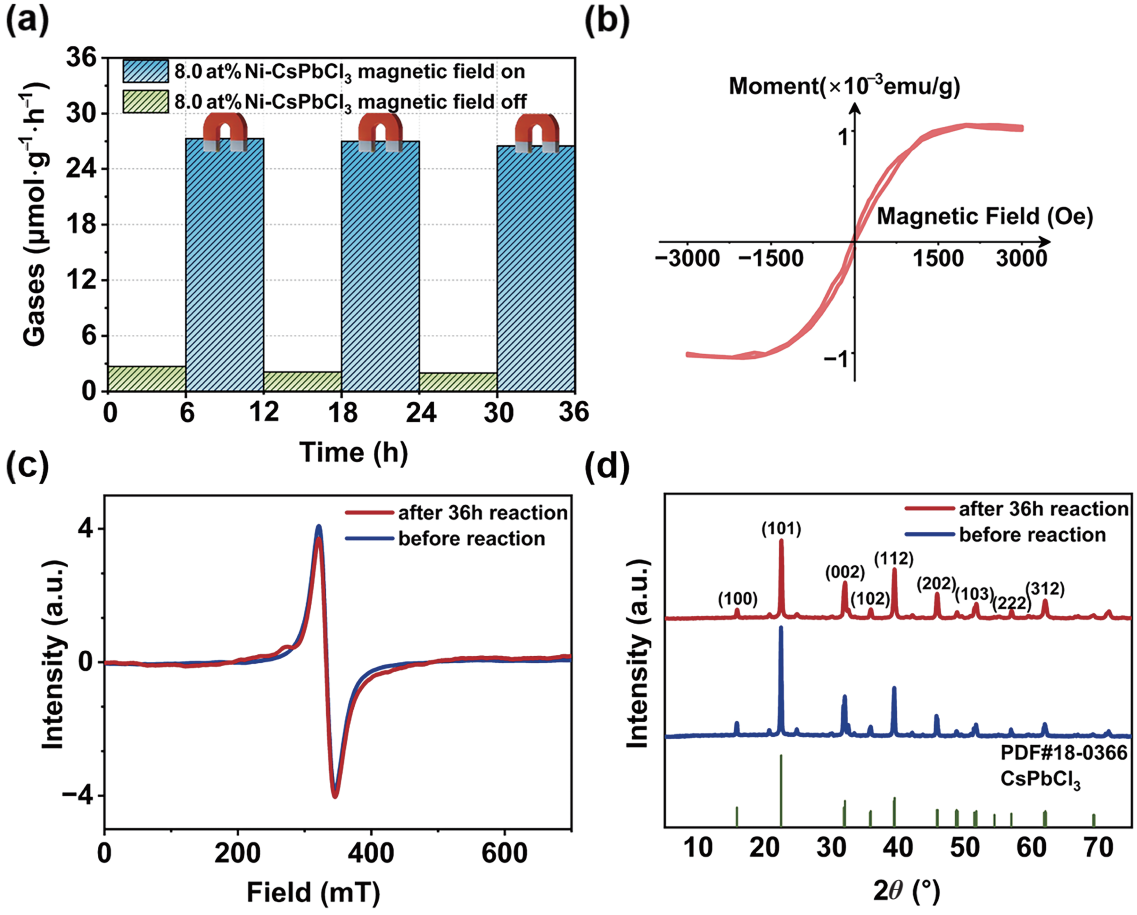

Fig. 4. (a) Changes in the photocatalytic yield with switching the magnetic field on or off. (b) Hysteresis loop of Ni-$CsPbCl_3$ with a nickel doping ratio of 8.0 at%. (c) EPR spectra and (d) XRD patterns of Ni-$CsPbCl_3$ with a nickel doping ratio of 8.0 at% before and after photocatalysis.

CSTR: 32290.14.JUSTC-2024-0078
DOI: 10.52396/JUSTC-2024-0078
JUSTC, **2024**, 54(9): 0902

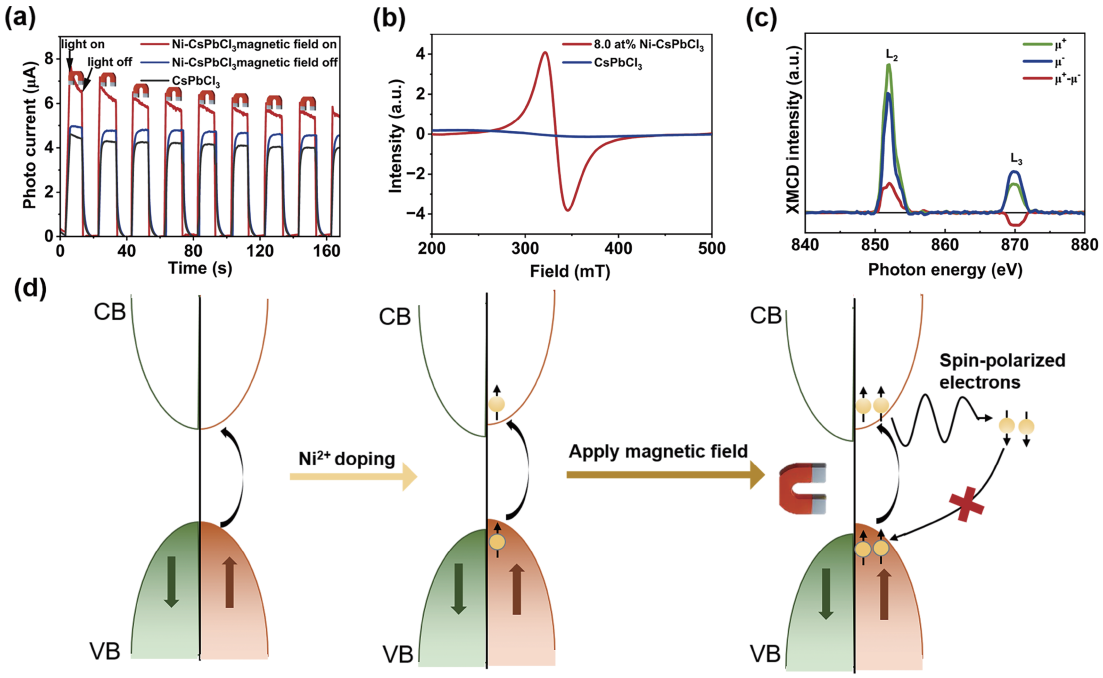

Fig. 5. (a) Photogenerated currents for $CsPbCl_3$ and Ni-$CsPbCl_3$ with a Ni doping ratio of 8.0 at%. (b) EPR spectra of $CsPbCl_3$ and Ni-$CsPbCl_3$ with a Ni doping ratio of 8.0 at%. (c) XMCD spectra of Ni-$CsPbCl_3$ with a Ni doping ratio of 8.0 at%. (d) Schematic diagram illustrating the mechanism of magnetic field-induced CO_2RR performance enhancement.

of approximately 2, whereas $CsPbCl_3$ presents no detectable EPR signal (Fig. 5b). This finding suggests that doping $CsPbCl_3$ with magnetic Ni^{2+} will make the catalyst paramagnetic and respond quickly to the magnetic field, thereby influencing the CO_2RR process[49]. Further investigations were conducted via X-ray magnetic circular dichroism (XMCD) spectroscopy under a magnetic field. The XMCD spectrum of Ni-$CsPbCl_3$ demonstrates the inherent spin-polarized band structure of the catalyst after Ni^{2+} doping and the enhanced splitting of the spin-polarized bands after the application of a magnetic field (Fig. 5c)[50]. These results confirm that an external magnetic field significantly enhances spin polarization in photoexcited carriers of Ni-$CsPbCl_3$, improving photocatalytic performance[51,52]. Through the above studies, the magnetic field-induced CO_2RR performance enhancement mechanisms are summarized in Fig. 5d. In semiconductor photocatalysis, illumination drives electrons from the valence band (VB) to the conduction band (CB), producing photogenerated electrons and corresponding holes. Typically, the random orientation of these electron spins leads to high recombination rates among electrons and holes with matching spins. After introducing Ni^{2+} into $CsPbCl_3$, the new electronic states from Ni^{2+} interact with the perovskite's existing electronic states, modifying its band structure. This interaction causes energy level splitting and the formation of spin-polarized bands, reducing recombination rates and potentially increasing carrier density, thereby increasing CO_2RR efficiency[49]. Applying an external magnetic field strengthens the splitting of the spin-polarized bands, leading to a further increase in spin-polarized electrons and holes[32,33], therefore decreasing the likelihood of recombination between photogenerated electrons and holes[53–56]. This reduction in recombination enhances the redox reactions essential for the CO_2RR in photocatalysts, thereby increasing the photocatalytic efficiency. This mechanism demonstrates that applying a magnetic field to Ni-$CsPbCl_3$ is an effective method for enhancing the photocatalytic CO_2 reduction efficiency.

4 Conclusions

In summary, a Ni-doped spin-polarized halide perovskite, Ni-$CsPbCl_3$, was synthesized in this work. The application of a magnetic field substantially enhances the photocatalytic CO_2RR efficiency of Ni-$CsPbCl_3$, primarily because increased spin polarization significantly reduces carrier recombination rates. Notably, this magnetic field is noncontact and easy to implement. This strategy capitalizes on the synergistic effects of magnetic fields and Ni doping to improve photocatalytic performance, opening new possibilities for the development of efficient and versatile photocatalysts. The design and application of magnetic fields and magnetic photocatalysts have broad prospects in the field of solar energy conversion.

Supporting information

The supporting information for this article can be found online at https://doi.org/10.52396/JUSTC-2024-0078. The supporting information includes seven figures and two tables.

Acknowledgements

This work was supported by the National Key R&D Program of China (2021YFA1501003), the Joint Funds of the National Natural Science Foundation of China (U23A2081), the National Natural Science Foundation of China (92261105, 22221003), the Anhui Provincial Key Research and

CSTR: 32290.14.JUSTC-2024-0078
DOI: 10.52396/JUSTC-2024-0078
JUSTC, **2024**, 54(9): 0902

Development Project (2023z04020010, 2022a05020053), the Anhui Provincial Natural Science Foundation (2108085UD06, 2208085UD04), the USTC Research Funds of the Double First Class Initiative (YD2060002029, YD2060006005), the Fundamental Research Funds for the Central Universities (WK2060000004, WK2060000021, WK2060000025, WK9990000155), and the Joint Funds from Hefei National Synchrotron Radiation Laboratory (KY2060000180, KY2060000195). We acknowledge the Experimental Center of Engineering and Material Science at the University of Science and Technology of China. We thank BL12B at the National Synchrotron Radiation Laboratory (NSRL) for assisting with characterization.

Conflict of interest

The authors declare that they have no conflict of interest.

Biographies

Zhiwen Zhang is currently pursuing her master's degree in Energy Chemistry at the University of Science and Technology of China. She received her B.S. degree from the University of Science and Technology of China in 2021. Her research mainly focuses on photocatalytic carbon dioxide reduction.

Yu Zhang is currently a specially-appointed associate research fellow at the University of Science and Technology of China. She received her Ph.D. degree from Kyoto University in 2020. Her research mainly focuses on electrocatalysis and photocatalysis.

Yuen Wu is currently a Professor at the University of Science and Technology of China. He received his B.S. and Ph.D. degrees from the Department of Chemistry, Tsinghua University, in 2009 and 2014, respectively. His research interests include the synthesis, assembly, characterization, and application exploration of single atom catalysts

References

[1] Goeppert A, Czaun M, Jones J P, et al. Recycling of carbon dioxide to methanol and derived products – closing the loop. *Chemical Society Reviews*, **2014**, *43* (23): 7995–8048.

[2] Kong T, Jiang Y, Xiong Y. Photocatalytic CO_2 conversion: What can we learn from conventional CO_x hydrogenation. *Chemical Society Reviews*, **2020**, *49* (18): 6579–6591.

[3] Meinshausen M, Meinshausen N, Hare W, et al. Greenhouse-gas emission targets for limiting global warming to 2 °C. *Nature*, **2009**, *458*: 1158–1162.

[4] Mikkelsen M, Jørgensen M, Krebs F C. The teraton challenge. A review of fixation and transformation of carbon dioxide. *Energy & Environmental Science*, **2010**, *3* (1): 43–81.

[5] Jiang Z, Sun H, Wang T, et al. Nature-based catalyst for visible-light-driven photocatalytic CO_2 reduction. *Energy & Environmental Science*, **2018**, *11* (9): 2382–2389.

[6] Fang S, Rahaman M, Bharti J, et al. Photocatalytic CO_2 reduction. *Nature Reviews Methods Primers*, **2023**, *3*: 61.

[7] Gong E, Ali S, Hiragond C B, et al. Solar fuels: research and development strategies to accelerate photocatalytic CO_2 conversion into hydrocarbon fuels. *Energy & Environmental Science*, **2022**, *15* (3): 880–937.

[8] He Y X, Yin L, Yuan N N, et al. Adsorption and activation, active site and reaction pathway of photocatalytic CO_2 reduction: A review. *Chemical Engineering Journal*, **2024**, *481*: 148754.

[9] Kojima A, Teshima K, Shirai Y, et al. Organometal halide perovskites as visible-light sensitizers for photovoltaic cells. *Journal of the American Chemical Society*, **2009**, *131* (17): 6050–6051.

[10] Hou Y, Aydin E, De Bastiani M, et al. Efficient tandem solar cells with solution-processed perovskite on textured crystalline silicon. *Science*, **2020**, *367* (6482): 1135–1140.

[11] Peng J, Kremer F, Walter D, et al. Centimetre-scale perovskite solar cells with fill factors of more than 86 per cent. *Nature*, **2022**, *601*: 573–578.

[12] San Martin J, Dang N, Raulerson E, et al. Perovskite photocatalytic CO_2 reduction or photoredox organic transformation. *Angewandte Chemie International Edition*, **2022**, *61* (39): e202205572.

[13] Kim T H, Cho K, Lee S H, et al. Spin polarization in Fe-doped $CsPbBr_3$ perovskite nanocrystals for enhancing photocatalytic CO_2 reduction. *Chemical Engineering Journal*, **2024**, *492*: 152095.

[14] Guo S N, Wang D, Wang J X. ZIF-8@$CsPbBr_3$ nanocrystals formed by conversion of Pb to $CsPbBr_3$ in bimetallic MOFs for enhanced photocatalytic CO_2 reduction. *Small Methods*, **2024**, *8* (10): 2301508.

[15] Jiang Y, Chen H Y, Li J Y, et al. Z-scheme 2D/2D heterojunction of $CsPbBr_3/Bi_2WO_6$ for improved photocatalytic CO_2 reduction. *Advanced Functional Materials*, **2020**, *30* (50): 2004293.

[16] Xu Y F, Yang M Z, Chen B X, et al. A $CsPbBr_3$ perovskite quantum dot/graphene oxide composite for photocatalytic CO_2 reduction. *Journal of the American Chemical Society*, **2017**, *139* (16): 5660–5663.

[17] Li Z J, Hofman E, Li J, et al. Photoelectrochemically active and environmentally stable $CsPbBr_3/TiO_2$ core/shell nanocrystals. *Advanced Functional Materials*, **2018**, *28* (1): 1704288.

[18] Ou M, Tu W, Yin S, et al. , Amino-assisted anchoring of $CsPbBr_3$ perovskite quantum dots on porous g-C_3N_4 for enhanced photocatalytic CO_2 reduction. *Angewandte Chemie International Edition*, **2018**, *57* (41): 13570–13574.

[19] Jiang Y, Liao J F, Chen H Y, et al. All-solid-state Z-scheme α-Fe_2O_3/amine-RGO/$CsPbBr_3$ hybrids for visible-light-driven photocatalytic CO_2 reduction. *Chem*, **2020**, *6* (3): 766–780.

[20] Sun Q M, Xu J J, Tao F F, et al. Boosted inner surface charge transfer in perovskite nanodots@mesoporous titania frameworks for efficient and selective photocatalytic CO_2 reduction to methane. *Angewandte Chemie International Edition*, **2022**, *61* (20): e202200872.

[21] Wang J C, Wang J, Li N Y, et al. Direct Z-scheme 0D/2D heterojunction of $CsPbBr_3$ quantum dots/Bi_2WO_6 nanosheets for efficient photocatalytic CO_2 reduction. *ACS Applied Materials & Interfaces*, **2020**, *12* (28): 31477–31485.

[22] Wang Q S, Yuan Y C, Li C F, et al. Research progress on photocatalytic CO_2 reduction based on perovskite oxides. *Small*, **2023**, *19* (38): 2301892.

[23] Cheng S, Zhao S D, Xing B L, et al. Facile one-pot green synthesis of magnetic separation photocatalyst-adsorbent and its application. *Journal of Water Process Engineering*, **2022**, *47*: 102802.

[24] Wang X D, Huang Y H, Liao J F, et al. In situ construction of a Cs_2SnI_6 perovskite nanocrystal/SnS_2 nanosheet heterojunction with boosted interfacial charge transfer. *Journal of the American Chemical Society*, **2019**, *141* (34): 13434–13441.

[25] Xu F Y, Meng K, Cheng B, et al. Unique S-scheme heterojunctions in self-assembled TiO_2/$CsPbBr_3$ hybrids for CO_2 photoreduction. *Nature Communications*, **2020**, *11*: 4613.

[26] Wu J K, Li Q F, Xue G B, et al. Preparation of single-crystalline heterojunctions for organic electronics. *Advanced Materials*, **2017**, *29* (14): 1606101.

[27] Wang Y, Li J Y, Zhou Y, et al. Interfacial defect mediated charge carrier trapping and recombination dynamics in TiO_2-based nanoheterojunctions. *Journal of Alloys and Compounds*, **2021**, *872*: 159592.

[28] Cho J Y, Kim S, Nandi R, et al. Achieving over 4% efficiency for SnS/CdS thin-film solar cells by improving the heterojunction

CSTR: 32290.14.JUSTC-2024-0078
DOI: 10.52396/JUSTC-2024-0078
JUSTC, **2024**, 54(9): 0902

interface quality. *Journal of Materials Chemistry A*, **2020**, *8* (39): 20658–20665.
[29] Frechette L B, Dellago C, Geissler P L. Consequences of lattice mismatch for phase equilibrium in heterostructured solids. *Physical Review Letters*, **2019**, *123* (13): 135701.
[30] Pan H P, Jiang X X, Wang X K, et al. Effective magnetic field regulation of the radical pair spin states in electrocatalytic CO_2 reduction. *The Journal of Physical Chemistry Letters*, **2020**, *11* (1): 48–53.
[31] Pan L, Ai M H, Huang C Y, et al. Manipulating spin polarization of titanium dioxide for efficient photocatalysis. *Nature Communications*, **2020**, *11*: 418.
[32] Dhanalakshmi R, Muneeswaran M, Vanga P R, et al. Enhanced photocatalytic activity of hydrothermally grown $BiFeO_3$ nanostructures and role of catalyst recyclability in photocatalysis based on magnetic framework. *Applied Physics A*, **2015**, *122* (1): 13.
[33] Gao W Q, Lu J B, Zhang S, et al. Suppressing photoinduced charge recombination via the Lorentz force in a photocatalytic system. *Advanced Science*, **2019**, *6* (18): 1901244.
[34] Li F, Cheng L, Fan J J, et al. Steering the behavior of photogenerated carriers in semiconductor photocatalysts: a new insight and perspective. *Journal of Materials Chemistry A*, **2021**, *9* (42): 23765–23782.
[35] Kodaimati M S, Gao R, Root S E, et al. Magnetic fields enhance mass transport during electrocatalytic reduction of CO_2. *Chem Catalysis*, **2022**, *2* (4): 797–815.
[36] Zhong S Y, Guo X L, Zhou A, et al. Fundamentals and recent progress in magnetic field assisted CO_2 capture and conversion. *Small*, **2024**, *20* (5): 2305533.
[37] He M L, Cheng Y Z, Shen L L, et al. Mn-doped $CsPbCl_3$ perovskite quantum dots (PQDs) incorporated into silica/alumina particles used for WLEDs. *Applied Surface Science*, **2018**, *448*: 400–406.
[38] Zhang R, Chen G, Liu H Y, et al. Synergetic effects of the co-doping transition metal ions and the silica-shell coating for enhancing the photoluminescence and stability of Mn:$CsPbCl_3$ nanocrystals and their application. *Optical Materials*, **2023**, *135*: 113308.
[39] Yu H Q, Gao X, Huang C C, et al. $CsPbCl_3$ and Mn:$CsPbCl_3$ perovskite nanocubes/nanorods as a prospective cathode material for LIB application. *Journal of Materials Science: Materials in Electronics*, **2023**, *34* (21): 1582.
[40] Cao Z, Li J, Wang L, et al. Enhancing luminescence of intrinsic and Mn doped $CsPbCl_3$ perovskite nanocrystals through Co^{2+} doping. *Materials Research Bulletin*, **2020**, *121*: 110608.
[41] Bagus P S, Nelin C J, Brundle C R, et al. Main and satellite features in the Ni 2p XPS of NiO. *Inorganic Chemistry*, **2022**, *61* (45): 18077–18094.
[42] Sakamoto K, Hayashi F, Sato K, et al. XPS spectral analysis for a multiple oxide comprising NiO, TiO_2, and $NiTiO_3$. *Applied Surface Science*, **2020**, *526*: 146729.
[43] Yu L C, Wei Y C, Lei Y C, et al. Achieving intrinsic dual-band excitonic luminescence from a single three-dimensional perovskite nanoparticle through Ni^{2+}-mediated halide anion exchange. *CCS Chemistry*, **2024**, *6* (2): 415–426.
[44] Zhang R, Yuan Y X, Zhang J F, et al. Improving the Mn^{2+} emission and stability of $CsPb(Cl/Br)_3$ nanocrystals by Ni^{2+} doping in ambient air. *Journal of Materials Science*, **2021**, *56* (12): 7494–7507.
[45] Mondal N, De A, Samanta A. Achieving near-unity photoluminescence efficiency for blue-violet-emitting perovskite nanocrystals. *ACS Energy Letters*, **2019**, *4* (1): 32–39.
[46] Pan G C, Bai X, Xu W, et al. Bright blue light emission of Ni^{2+} ion-doped $CsPbCl_xBr_{3-x}$ perovskite quantum dots enabling efficient light-emitting devices. *ACS Applied Materials & Interfaces*, **2020**, *12* (12): 14195–14202.
[47] De A, Mondal N, Samanta A. Luminescence tuning and exciton dynamics of Mn-doped $CsPbCl_3$ nanocrystals. *Nanoscale*, **2017**, *9* (43): 16722–16727.
[48] Klein J, Kampermann L, Mockenhaupt B, et al. Limitations of the Tauc plot method. *Advanced Functional Materials*, **2023**, *33* (47): 2304523.
[49] De Siena M C, Sommer D E, Creutz S E, et al. Spinodal decomposition during anion exchange in colloidal Mn^{2+}-doped $CsPbX_3$ (X = Cl, Br) perovskite nanocrystals. *Chemistry of Materials*, **2019**, *31* (18): 7711–7722.
[50] Antonov V N, Bekenov L V, Uba S, et al. Electronic structure and X-ray magnetic circular dichroism in the Ni-Mn-Ga Heusler alloys. *Journal of Alloys and Compounds*, **2017**, *695*: 1826–1837.
[51] Feng S H, Duan H L, Tan H, et al. Intrinsic room-temperature ferromagnetism in a two-dimensional semiconducting metal-organic framework. *Nature Communications*, **2023**, *14*: 7063.
[52] Hu J X, Han Y L, Chi X, et al. Tunable spin-polarized states in graphene on a ferrimagnetic oxide insulator. *Advanced Materials*, **2024**, *36* (8): 2305763.
[53] Wang Y, Wang S L, Wu Y B, et al. A α-Fe_2O_3/rGO magnetic photocatalyst: Enhanced photocatalytic performance regulated by magnetic field. *Journal of Alloys and Compounds*, **2021**, *851*: 156733.
[54] Liu D, Huang Y J, Hu J W, et al. Multiscale catalysis under magnetic fields: methodologies, advances, and trends. *ChemCatChem*, **2022**, *14* (24): e202200889.
[55] Li X B, Wang W W, Dong F, et al. Recent advances in noncontact external-field-assisted photocatalysis: from fundamentals to applications. *ACS Catalysis*, **2021**, *11* (8): 4739–4769.
[56] He J, Wang Y, Shi C J, et al. Enhanced performance of a magnetic photocatalyst regulated using a magnetic field. *Separation and Purification Technology*, **2022**, *284*: 120263.

CSTR: 32290.14.JUSTC-2024-0078
DOI: 10.52396/JUSTC-2024-0078
JUSTC, **2024**, 54(9): 0902